Heliyon

ELSEVIER

Received:
19 October 2016
Revised:
12 January 2017
Accepted:
24 January 2017

Heliyon 3 (2017) e00239

Non-parametric intravoxel incoherent motion analysis of the thyroid gland

Anton S. Becker *, Moritz C. Wurnig, Tim Finkenstaedt, Andreas Boss

Institute of Diagnostic and Interventional Radiology, University Hospital of Zurich, Switzerland

* Corresponding author at: Department of Radiology, University Hospital of Zurich, Raemistrasse 100, Switzerland.
E-mail address: anton.becker@usz.ch (A.S. Becker).

Abstract

Purpose: To implement a protocol for intravoxel incoherent motion (IVIM) of the thyroid, to determine base parameters in healthy volunteers, and to provide preliminary experience on clinical applicability in one patient.

Materials and methods: Eight healthy volunteers underwent 3T MRI using a diffusion weighted echo-planar imaging sequence with 12 different b-values between 0–800 s/mm^2. The IVIM parameters diffusion coefficient D, pseudo-diffusion coefficient D*, perfusion fraction F_p, and the optimal b-values thresholds were calculated for each thyroid lobe, muscle tissue and the cerebrospinal fluid (CSF) using a non-parametric multi-step algorithm and compared with a Student's t-test. A p-value <0.05 was considered significant.

Results: Mean values for healthy thyroid tissue were: D $1.01 \pm 0.13 \times 10^{-3}$ mm^2/s, D* $71.0 \pm 52.5 \times 10^{-3}$ mm^2/s and F_p $17.1 \pm 4.2\%$; for muscle: D $0.50 \pm 0.21 \times 10^{-3}$ mm^2/s, D* $58.3 \pm 99.2 \times 10^{-3}$ mm^2/s and F_p $26.5 \pm 9.3\%$; and for CSF D $2.18 \pm 0.93 \times 10^{-3}$ mm^2/s, D* $99.2 \pm 41.2 \times 10^{-3}$ mm^2/s and F_p $74.6 \pm 12.7\%$. The optimal b-value threshold separating diffusion and perfusion effects in thyroid ranged between 0–70 s/mm^2. Healthy thyroid tissue showed similar F_p compared to muscle, both lower than CSF.

Conclusions: The proposed IVIM protocol provides surrogate markers on cellular diffusion restriction and perfusion; thereby providing a more comprehensive description of tissue properties compared to conventional DWI.

Keywords: Physiology, Anatomy, Medicine, Medical imaging, Pathology

http://dx.doi.org/10.1016/j.heliyon.2017.e00239

2405-8440/© 2017 The Authors. Published by Elsevier Ltd. This is an open access article under the CC BY-NC-ND license (http://creativecommons.org/licenses/by-nc-nd/4.0/).

1. Introduction

Thyroid nodules are some of the most common incidentally reported lesions in radiology with a reported prevalence of up to 67% [1] especially in geographic areas with low iodine in the everyday diet [2]. The vast majority of incidental thyroid nodules, particularly when small in size (defined as <1 cm), are benign in nature ("regressive changes") and need no treatment or follow up [3]. However, a small percentage of nodules represent thyroid carcinomas. When detected early, the differentiated papillary and follicular thyroid carcinomas (the two most common types) are well treatable with radiotherapy and/or surgery, with a 30-year cancer death rate of only 8% and a recurrence rate of 30% [4]. Medullary and anaplastic thyroid cancer however, are often only diagnosed in later stages and represent very aggressive types of cancer, with overall median survival limited to only several months [5]. Thus, accurate differentiation of thyroid findings is of paramount importance for the early detection and appropriate treatment of thyroid cancer.

Ultrasonography and ^{131}Iodine- or ^{99m}Technetium-scintigraphy are the main diagnostic modalities used in thyroid nodule workup [6]. Ultrasonography in the clinical routine is only able to deliver anatomical; and, apart from Doppler-sonography for vascularity, no functional information about the tissue is provided. Classic imaging features such as calcifications, shape and contrast enhancement are fairly non-specific [7], neither can dynamic contrast enhanced CT differentiate between benign and malignant nodules [8]. Contrast enhanced sonography with ligand targeted contrast media ("microbubbles") is an interesting novel approach to add metabolic or molecular information to the modality [9]; however, it is still only in an experimental stage and has not been approved for routine clinical usage. As an additional drawback, ultrasonography is heavily operator-dependent [10]. Scintigraphy on the other hand yields excellent functional information, but has poor spatial resolution and is associated with a substantial radiation dose to the whole body and the thyroid gland in particular, due to local accumulation of the ^{131}I- or ^{99m}Tc isotopes and the relatively high natural radiosensitivity of the thyrocytes [11, 12].

MRI somewhat unifies advantages of both modalities, with the ability to objectively examine the anatomy with rather high spatial resolution and intrinsic high soft tissue contrast while also providing functional information about the tissue [13] without use of ionizing radiation. Quantitative diffusion weighted MRI has been shown to correlate with the hypercellularity in thyroid carcinomas [14]. However, detailed knowledge about the diffusion properties of healthy thyroid tissue as well as quantification of thyroid perfusion is essential in order to be able to discriminate between physiological and pathological changes.

http://dx.doi.org/10.1016/j.heliyon.2017.e00239
2405-8440/© 2017 The Authors. Published by Elsevier Ltd. This is an open access article under the CC BY-NC-ND license (http://creativecommons.org/licenses/by-nc-nd/4.0/).

MRI offers several non-invasive options to measure tissue perfusion. For instance, arterial spin labeling (ASL) has been shown to reliably generate single-slice perfusion maps of the thyroid gland with a flow-sensitive alternating inversion-recovery spin preparation and a true fast imaging in steady precession technique [15] and was subsequently used to quantify perfusion changes in Hashimoto thyroiditis [16]. Yet, precise perfusion quantification with ASL is difficult due to the signal contribution of intravascular tagged spins, early magnetization decay of tagged spins and a low signal-to-noise ratio (SNR).

Alternatively intravoxel incoherent motion (IVIM) imaging has recently been proven to be a reliable tool providing tissue characteristics on cellularity as well as perfusion-dependent biomarkers [17]. The principle behind IVIM was first postulated in 1988 by Le Bihan et al. [18].

The aim of this study was to optimize and implement an MRI protocol allowing for acquisition of diffusion datasets suitable for IVIM analysis of the thyroid gland, to test a parameter-free post-processing algorithm for IVIM analysis in healthy volunteers, to report baseline parameters of healthy volunteers, as well as an anecdotal example of a benign focal pathology (autonomous adenoma) in one patient.

2. Materials and methods

2.1. Study cohort

The study was approved by the institutional review board. The population consisted of nine volunteers in total: Eight healthy volunteers (5 male, 3 female; 28.3 ± 5.1 years old), and one (female, 55y) with a known autonomous adenoma in the left thyroid lobe. Oral and written informed consent was obtained.

2.2. MRI protocol

All MRI scans were performed on a clinical 3.0T MRI scanner (Ingenia, Philips Healthcare, Best, NL). Subjects were laid in supine position in a 15-channel head & neck coil. Room temperature was kept at a constant 21 °C. All sequences were acquired perpendicular to the axis of the spinal column ("transverse" or "axial" orientation). In a first step, T1/T2 weighted fast spin echo (FSE) sequences (field of view 22 × 22 × 29 cm, voxel size 0.85 × 0.85 mm/0.76 × 0.76 mm, no. of slices 40, slice thickness 4 mm, slice spacing 3.3 mm, T_R and T_E of 580 and 18 ms/3400 and 90 ms, flip angle 90°, acquisition time 4:20 min) were acquired in order to gain sufficient anatomical information about the region to a) plan the acquisition of the diffusion weighted images precisely over the thyroid and b) screen for structural abnormalities that would alter the DWI measurements (eg. cysts or large regressive nodules). In a second step, a DWI sequence using single-shot spin-echo echo-planar imaging with signal averaging in three orthogonal directions was applied

http://dx.doi.org/10.1016/j.heliyon.2017.e00239
2405-8440/© 2017 The Authors. Published by Elsevier Ltd. This is an open access article under the CC BY-NC-ND license (http://creativecommons.org/licenses/by-nc-nd/4.0/).

(field of view 20 × 20 × 17.6 cm, voxel size 1.39 × 1.39 mm, no. of slices 22, slice thickness 3.5 mm, slice spacing 4.5 mm, T_R 5000 ms, T_E 69 ms, bandwidth 1.8 kHz, fat suppression by spectral attenuated inversion recovery (SPAIR), b-values: 0, 10, 20, 40, 70, 100, 150, 300, 400, 500, 650, 800 s/mm^2; Sensitivity Encoding (SENSE) factor 2, acquisition time 25:15 min). A typical example of the sequence planning and representative diffusion images are presented in Fig. 1.

2.3. Post-processing

IVIM exploits a so-called "pseudodiffusion-effect" which corresponds to fast moving water molecules in the capillaries [18, 19, 20]. This effect will, depending on the tissue, superimpose the signal decay caused by true diffusion. It is typically observed at low b-values (<150 s/mm^2). The phenomenon can be described by a bi-exponential equation:

$$Sb/S0 = (1 - Fp)exp(-bD) + Fpexp(-bD*) \quad (1)$$

In the above equation, S represents the signal, D the apparent molecular diffusion, D* the pseudodiffusion and F_p the relative perfusion fraction. In the brain, the

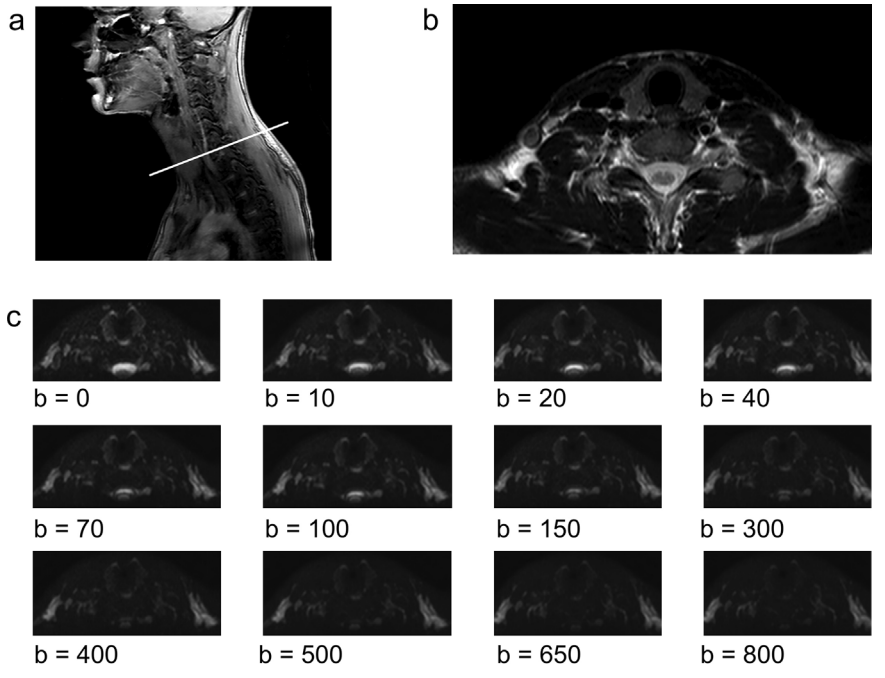

Fig. 1. (a) T2 weighted anatomical sequence, sagittal slice in paramedian position through the neck of a healthy volunteer. The white line depicts the axial orientation of the subsequent acquired images and the position of (b) an anatomical axial T2 weighted image through the neck with no structural abnormalities. (c) diffusion weighted images with the 12 different b-values later used for IVIM analysis. Note the rapid and consistent signal decay (0 to 800, from hyper- to hypointense) in the CSF consistent with near-free diffusivity. The signal values in all images range from 0 to 1 (black to white, gray scale omitted).

http://dx.doi.org/10.1016/j.heliyon.2017.e00239
2405-8440/© 2017 The Authors. Published by Elsevier Ltd. This is an open access article under the CC BY-NC-ND license (http://creativecommons.org/licenses/by-nc-nd/4.0/).

product $F_p \times D^*$ has been shown to linearly correlate with the blood flow measured after bolus contrast injection [20, 21].

Proprietary built-in automatic three-dimensional motion correction was successfully applied to all images ("diffusion registration" package, Philips Healthcare). All IVIM-analyses were performed with optimized in-house MATLAB (MathWorks, Natick MA, USA) computer programs.

Polygonal regions of interest (ROIs) were manually placed in each lobe of the thyroid, the sternocleidomastoid muscle and the cerebrospinal fluid (CSF) in the cervical spinal canal. While drawing the ROIs, inclusion of large vessels such as the internal jugular vein or carotid artery were avoided, and were not placed in close proximity to the extracorporal or tracheal airspaces, to minimize distortive effects from pulsation or susceptibility artifacts. Any necrotic regions were avoided as well in order to minimize the influence of potential measurement errors. The ROIs were placed on the b_0 slice with the best visibility of all structures in question (thyroid parenchyma, muscle and CSF) and automatically copied to the images of the remaining 11 b-values, generating a decay curve comprising 12 measurement points (x = b-value/y = signal-intensity). ROI definition was performed by two readers independently (AB, 3 years and TF, 5 years of experience in clinical MRI), and by one of the readers (AB) after >6 months, to assess inter- and intrareader agreement, respectively. For the IVIM analysis a multi-step variable b-value threshold fitting approach was used, which has been shown to deliver more consistent results than conventional bi-linear fitting [22]. Our approach consists of the routine:

1.) D is calculated from the highest n b-values with the assumption, that perfusion contributions to the signal decay are negligible at high b-values. Initially, n is equal to the number of b-values. D is calculated using a first-order polynomial fit to the log-transformed signal intensities:

$$logS_b = -D \times b + logS_0' \tag{2}$$

2.) The perfusion fraction F_p is subsequently calculated from the measured signal intensity at b = 0 (S_0) and the derived S_0':

$$F_p = \frac{S_0 - S_0'}{S_0} \tag{3}$$

3.) Using the computed values for D and F_p as fixed factors, D* is determined for all b-values by fitting the signal intensities to Eq. (1) using a non-linear least-sqaures algorithm based on the Levenberg-Marquardt technique. The corresponding MATLAB function "lsqcurvefit" also provides the sum of the squared residuals to the fit.

http://dx.doi.org/10.1016/j.heliyon.2017.e00239
2405-8440/© 2017 The Authors. Published by Elsevier Ltd. This is an open access article under the CC BY-NC-ND license (http://creativecommons.org/licenses/by-nc-nd/4.0/).

4.) Steps 1–3 are repeated with the next lower b-value dropped in step 1 and 2 to determine the initial D and F_p. Therefore, the algorithm will loop n-1 times through the data with n equal to the number of b-values acquired. In the end, only the two highest b-values remain as for the highest b-value alone no polynomial fit can be calculated.

5.) Lastly, the optimal b-value threshold and resulting IVIM-parameters can be determined by using the b-value threshold with the corresponding lowest number of squared residuals from step 3, equaling the best fit to the measured signal intensities.

In addition to the ROI analysis, voxel-wise IVIM analysis of the selected slices was done to generate parametrical b-value threshold, F_p-, D- and D*-maps of the whole examined region, which were digitally fused with the corresponding b_0 DWI-image, as a visual instrument to verify the quantitative measurements obtained by the ROI analysis.

2.4. Statistical analysis

Statistical analysis was performed using R v. 3.3.1. (R Foundation for Statistical Computing, Vienna, Austria). ROI size was expressed as median and interquartile range (IQR). For all 9 subjects, the optimal b-value threshold was determined for CSF, muscle and each thyroid lobe, as well as additionally an adenoma in one subject. The median of these b-value thresholds was calculated per structure. Means and standard deviations of the IVIM parameters F_p-, D- and D* were computed for each anatomical structure of all subjects at this median b-value. These results were compared with a Student t-test with Bonferroni correction for multiple comparisons, yielding $p = 0.05/3 = 0.017$ as an indicator of significant differences. All plots including an exemplary fitting process in the thyroid were plotted with ggplot2 from the raw MATLAB output (cf. Fig. 2). The 1 case of an autonomous adenoma was also compared to the mean and confidence intervals of the results from the healthy subjects. Intra- and interreader agreement/reliability were assessed with the intraclass correlation coefficient (ICC) and Bland-Altman plots, respectively. ICC values were interpreted as follows: poor (<0.20), fair (0.20–0.39), moderate (0.40–0.59), substantial (0.60–0.79), and excellent (>0.80) agreement.

3. Results

3.1. Qualitative and quantitative analysis of IVIM parameters in healthy subjects

The three examined anatomical compartments: Thyroid, muscle and CSF showed distinct and consistent differences in the signal decay over the different b-values. Three exemplary decay curves are depicted in Fig. 2a, showing a faster signal decay in the CSF when compared to muscle and the thyroid gland. The thyroid

http://dx.doi.org/10.1016/j.heliyon.2017.e00239
2405-8440/© 2017 The Authors. Published by Elsevier Ltd. This is an open access article under the CC BY-NC-ND license (http://creativecommons.org/licenses/by-nc-nd/4.0/).

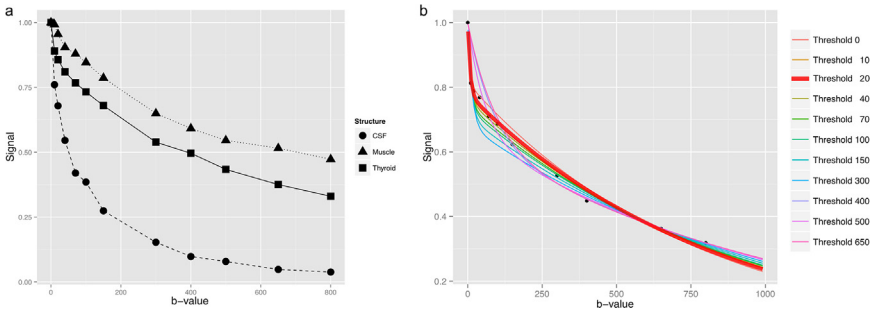

Fig. 2. (a) Measured signal from one of the volunteers showing a more rapid signal decay in the thyroid gland at very small b-values (<70) with subsequent equalization of the decay slope to muscle tissue leading to a nearly constant difference between the two curves. (b) Exemplary multi-step fitting approach on the thyroid signal data. Note the different scale. The optimal b-value threshold determined by the smallest sum of squared differences from the measured points to the curve was a b-value of 20 s/mm^2 highlighted in red and bold, which seems to optimally reflect the early steep signal decay.

gland exhibited a decay pattern in between CSF and muscle with a fast initial decay at b = 10–20 s/mm^2 similar to CSF, but after b = 70 almost paralleling the slow decay of the muscle-curve. The subsequent results of the fitting algorithm applied to the thyroid-curve of Fig. 2a is graphically depicted in Fig. 2b, where 11 IVIM fitting curves with increasing b-value thresholds were tested and according to step 5 of our routine the function with lowest residuals was selected as the optimal b-value threshold function (in this example threshold b-value 20, marked red and bold).

Median ROI size was 55 px (IQR: 46–71 px) for the left, 69 px (52–80 px) for the right thyroid, 130 px (124–138 px) for muscle and 37 px (32–73 px) for the CSF. The median optimal b-value thresholds were 40 and 20 s/mm^2 for the left and right thyroid lobe, 500 s/mm^2 for the skeletal muscle and 20 s/mm^2 for CSF (cf. Table 1). The thyroid gland showed a simlar F_p, compared to skeletal muscle (19.6% vs. 26.5%, $p = 0.12$). F_p was significantly higher in the spinal canal (74.6%, $p < 0.001$), probably corresponding to the physiological CSF-pulsation (Fig. 3a). Similarly, D* and D were high in CSF and low in the muscle ($p < 0.001$), consistent with the free water diffusion in the CSF and physiologically restricted diffusion in the parallel oriented muscle fibers. In contrast to F_p, D* and D of the parenchymatous thyroid gland exhibited values between the respective parameters of CSF and muscle (Fig. 3b and c). The small differences of the IVIM parameters F_p, D* and D between the two lobes of the thyroid gland were never significant (Fig. 3), indicating good reproducibility.

3.2. Parametrical maps of the healthy subjects

Fig. 4arepresents an exemplary section of a T2-weighted anatomical sequence, with Fig. 4b depicting the corresponding DWI section at b = 0 s/mm^2. The DWI image was used for the fusion with the parametric maps, since the DWI as well as

http://dx.doi.org/10.1016/j.heliyon.2017.e00239
2405-8440/© 2017 The Authors. Published by Elsevier Ltd. This is an open access article under the CC BY-NC-ND license (http://creativecommons.org/licenses/by-nc-nd/4.0/).

Table 1. Summary Table with means and standard deviations of the IVIM parameters for the examined structures, as well as the measurement for the singular adenoma. The perfusion fraction (F_p) of the thyroid was similar to muscle and lower than in the CSF. Whereas the diffusion coefficient (D) as well as the pseudodiffusion (D*) of the throid ranged between muscle and CSF. The adenoma showed markedly different IVIM parameters (ie. lower F_p, higher D and D*) compared to the healthy thyroid tissue. The b-value threshold is given as median [interquartile range], the remaining coefficients are expressed as mean ± standard deviation.

Parameter	Left Thyroid	Right Thyroid	Thyroid Adenoma	Muscle	CSF
n	8	8	1	9	9
F_p	22.1 ± 3.4%	17.1 ± 4.2%	3.0%	26.5 ± 9.3%	74.6 ± 12.7%
D* [$\times 10^{-3}$ mm^2/s]	64.2 ± 43.7	71.0 ± 52.5	95.2	58.3 ± 10.9	99.2 ± 41.2
D [$\times 10^{-3}$ mm^2/s]	0.96 ± 0.18	1.01 ± 0.13	2.28	0.50 ± 0.21	2.18 ± 0.93
Optimal b-Value [s/mm^2]	40 [20–40]	20 [10–70]	0	500 [500–650]	20 [20–20]

the maps showed small distortions due to magnetic field inhomogeneities, eg. in proximity to air-tissue interfaces, as can be seen in the isthmus of the thyroid gland. The maps were in concordance with the results from the quantitative measurements, depicting a low b-value threshold for thyroid gland and CSF and substantially higher b-value threhold for the muscles (Fig. 4c), high F_p in and around the spinal canal and lower in muscle and thyroid tissue (Fig. 4d) as well as intermediate D and D* in the thyroid when compared with CSF and muscles (Fig. 4e and f). The latter have shown the most inhomogeneous pattern of the examined structures. Additionally, a "hotspot" of high F_p and D* could be appreciated around the right internal jugular vein, probably corresponding to the slow macroscopic blood flow within this large vein in the supine position.

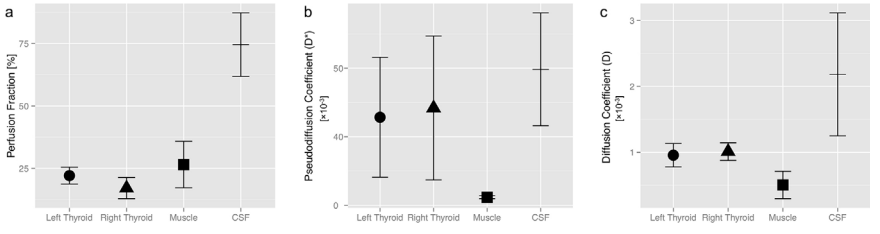

Fig. 3. (a) While the perfusion fraction F_p was not significantly different between thyroid and muscle tissue, the CSF, presumably through its physiological pulsation, showed a very high F_p. (b) The pseudodiffusion coefficient D* was relatively high in the thyroid and CSF with greater variability, when compared to the muscles. (c) Diffusion was nearly unrestricted in the CSF (high D), and less restricted in the loose thyroid parenchyma than in the tough muscle fibers (lowest D).

http://dx.doi.org/10.1016/j.heliyon.2017.e00239
2405-8440/© 2017 The Authors. Published by Elsevier Ltd. This is an open access article under the CC BY-NC-ND license (http://creativecommons.org/licenses/by-nc-nd/4.0/).

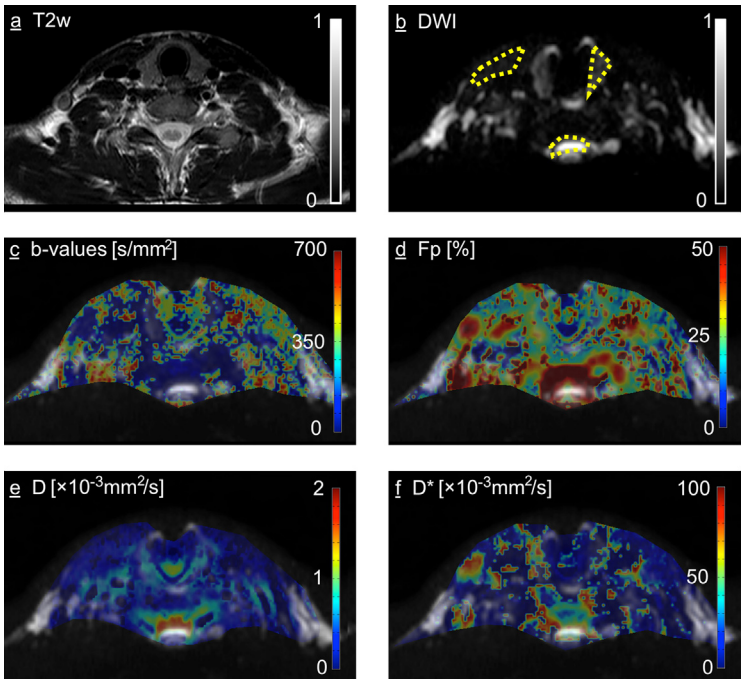

Fig. 4. (a) T2 weighted anatomical sequence, axial slice through the neck on the level of the thyroid (b) Diffusion weighted image with b-value = 0 s/mm^2, note the distortion of the thyroid isthmus due to its location between the extracorporal and tracheal air. Sample ROI definitions in the left thyroid, muscle and CSF are shown (dashed yellow lines). This image was used for the fusion with the parametric maps in (c–f) as determined in the by-voxel IVIM analysis: (c) Optimal b-value threshold (d) Perfusion fraction Fp [%] (e) Diffusion coefficient D [mm^2/s] (f) Pseudodiffusion coefficient D* [mm^2/s].

3.3. Quantitative and qualitative comparison with the autonomous adenoma

The adenoma showed the following imaging characteristics: Well demarcated, inhomogeneously iso- to slightly hyperintense on T1 and markedly hyperintense on T2 weighted anatomical sequences, as shown in Fig. 5a and b. The optimal threshold on the functional DWI sequences was found to be 0 s/mm^2, in the contralateral, normal lobe it was 20 s/mm^2 as shown in Fig. 5d, in congruency with the other, healthy thyroid glands. The resulting fitted curve was an almost mono-exponential signal decay from b_0 to b_{800}, depicted in Fig. 5g together with a normal thyroid decay curve. The decay is still not purely exponential, as this would require the line of the log transformed Consecutively, a very low F_p was detected (3.0% vs. 19.6%; Fig. 5e and h) and a relatively high diffusion coefficient D (2.2 vs. 0.98 × 10^{-3} mm^2/s; Fig. 5f and i); Table 1. Both parameters were well outside of the 99.7% confidence intervals of the respective parameter of the healthy thyroid gland. D* in the adenoma was only slightly higher than in the normal thyroid and well within the 95% confidence intervals.

http://dx.doi.org/10.1016/j.heliyon.2017.e00239
2405-8440/© 2017 The Authors. Published by Elsevier Ltd. This is an open access article under the CC BY-NC-ND license (http://creativecommons.org/licenses/by-nc-nd/4.0/).

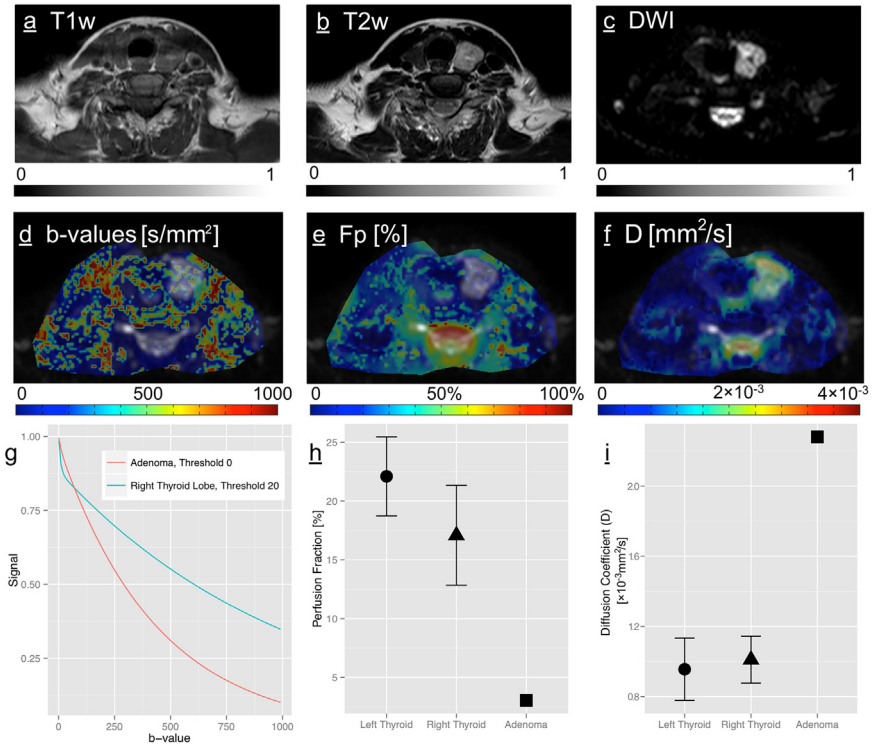

Fig. 5. (a) T1 weighted (b) T2 weighted anatomical sequence, axial slice through the neck on the level of the thyroid gland and adenoma. This adenoma had a typical MR appearance, isointense on T1 and hyperintense on T2 and consequently hyperintense on (c) the b_0 image. Below on (g) two exemplary fitted curves from the ROI analysis are shown, comparing healthy thyroid to the adenoma with markedly different signal decay characteristics, which is in turn reflected in (e) and (h) showing the low F_p and (f) and (i) the high D in the adenoma compared to the healthy thyroid tissue.

3.4. Intra- and interreader agreement

The first complete readout of Reader 1 is provided in Table 2. Intrareader agreement was excellent for Fp (ICC = 0.87, 95%-CI = 0.74–0.93) and substantial for D* (0.68, 0.38–0.84) and D (0.77, 0.54–0.88). Interreader analysis exhibited the same pattern with excellent agreement for Fp (0.93, 0.85–0.96) and substantial for D* (0.71, 0.45–0.85) and D (0.79, 0.59–0.89). Bland-Altman plots (Fig. 6) showed no gross deviation of the mean from zero in any case, confirming the results of the ICC analysis.

4. Discussion

In the present study we demonstrated that tissue characterization of the thyroid gland is feasible using an IVIM diffusion imaging approach, which provides biomarkers on restriction of water diffusion (cellularity) and perfusion (Table 1). Computation of parametrical maps provided a satisfying spatial resolution and image quality. Using a non-parametrical post-processing algorithm, the optimal b-

http://dx.doi.org/10.1016/j.heliyon.2017.e00239
2405-8440/© 2017 The Authors. Published by Elsevier Ltd. This is an open access article under the CC BY-NC-ND license (http://creativecommons.org/licenses/by-nc-nd/4.0/).

Table 2. Measured perfusion fraction (F_p), apparent and pseudo-diffusion coefficient (D and D*) for each structure examined in the ROI analysis for every healthy subject.

Structure	Subject	Optimal b-value [s/mm^2]	F_p [%]	D [$\times 10^{-3}$ mm^2/s]	D* [$\times 10^{-3}$ mm^2/s]
Left Thyroid	1	20	18.6	0.84	71.9
Left Thyroid	2	20	19.8	0.92	77.6
Left Thyroid	3	40	26.1	1.23	55.7
Left Thyroid	4	40	21.0	0.88	157.3
Left Thyroid	5	20	18.3	1.22	52.2
Left Thyroid	6	40	21.2	0.79	44.2
Left Thyroid	7	40	25.5	0.78	51.1
Left Thyroid	8	70	26.3	0.98	34.9
Right Thyroid	1	70	16.8	0.98	39.5
Right Thyroid	2	10	17.3	0.85	72.6
Right Thyroid	3	20	25.7	1.06	73.2
Right Thyroid	4	70	20.7	0.96	33.9
Right Thyroid	5	70	17.2	1.21	68.0
Right Thyroid	6	20	14.9	0.88	43.2
Right Thyroid	7	0	12.5	0.99	18.7
Right Thyroid	8	0	17.1	1.23	19.6
Muscle	1	500	20.3	0.38	58.9
Muscle	2	300	25.9	0.50	60.3
Muscle	3	650	41.1	0.20	50.4
Muscle	4	100	43.5	0.47	62.1
Muscle	5	500	22.0	0.58	57.2
Muscle	6	650	20.4	0.61	51.3
Muscle	7	500	22.1	0.40	45.9
Muscle	8	650	18.2	0.95	83.7
Cerebrospinal Fluid	1	70	60.5	4.02	39.8
Cerebrospinal Fluid	2	20	88.3	1.67	170.7
Cerebrospinal Fluid	3	20	82.6	1.56	100.3
Cerebrospinal Fluid	4	70	53.2	2.24	37.2
Cerebrospinal Fluid	5	10	74.2	3.00	87.7
Cerebrospinal Fluid	6	20	62.1	0.76	119.4
Cerebrospinal Fluid	7	20	83.9	1.76	116.4
Cerebrospinal Fluid	8	20	82.9	2.42	109.3

value for separation of perfusion and diffusion effects for healthy tissue could be determined to be in the range of 20–40 s/mm^2. Moreover, base parameters in a cohort of healthy volunteers could be obtained. Preliminary experience on the clinical applicability of the proposed protocol could be derived from a measurement in a patient with an autonomous adenoma.

http://dx.doi.org/10.1016/j.heliyon.2017.e00239
2405-8440/© 2017 The Authors. Published by Elsevier Ltd. This is an open access article under the CC BY-NC-ND license (http://creativecommons.org/licenses/by-nc-nd/4.0/).

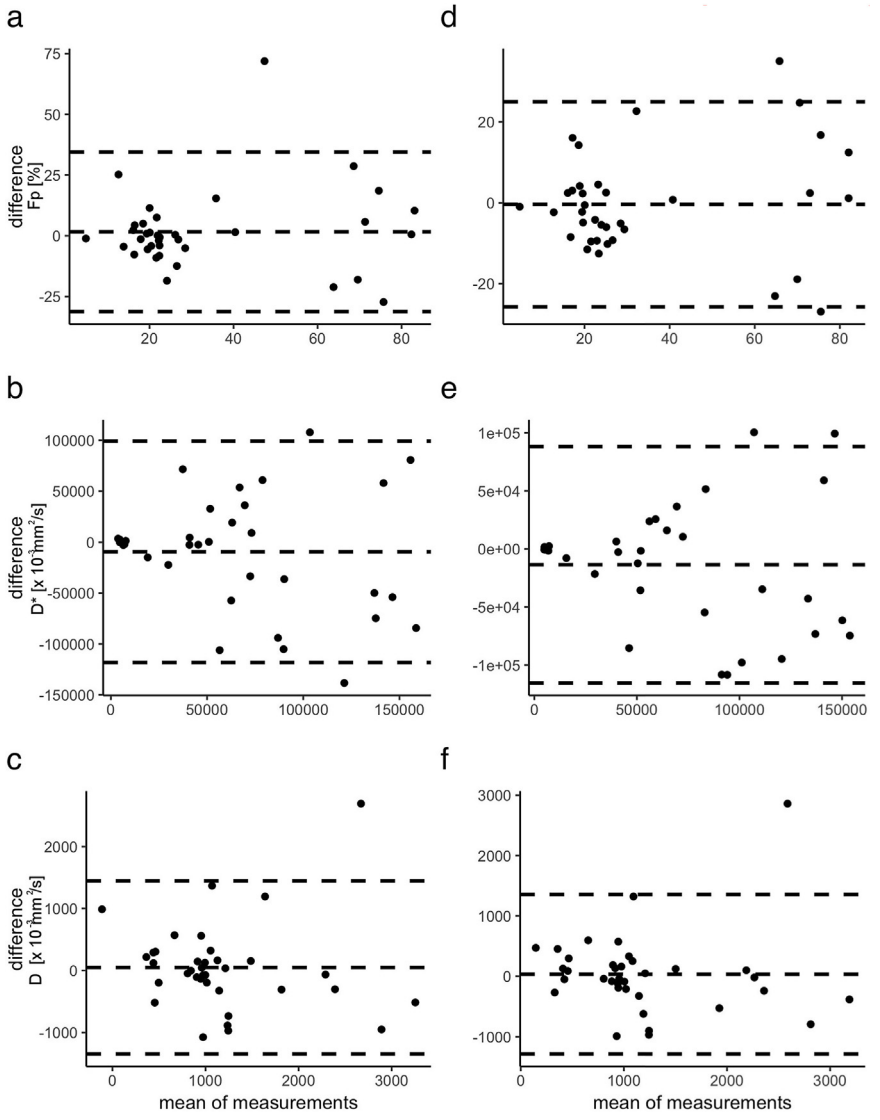

Fig. 6. Bland-Altman plots of the perfusion fraction Fp, the pseudodiffusion coefficient D* and the diffusion coefficient D (top to bottom) within the same reader after >6 months (intrareader analysis: a–c) and two separate readers (interreader analysis, d–f). Mean difference ± 1.96 SD are shown by the dashed lines. In none of the comparisons, the mean deviates far from zero, indicating no systematic bias in the readouts.

Of the examined structures, the different muscles showed the most inhomogeneous pattern on the parametric maps. This can partly be explained by different activity before and during the scan, which locally alters muscle perfusion and thus the measured IVIM parameters [23]. Some of the "hotspots" may be explained through slightly larger arterioles and venules coursing through the muscle. Another factor that may contribute to this picture is the different 3-dimensional muscle fiber orientation of the different muscle groups. IVIM does not take the directionality of

http://dx.doi.org/10.1016/j.heliyon.2017.e00239
2405-8440/© 2017 The Authors. Published by Elsevier Ltd. This is an open access article under the CC BY-NC-ND license (http://creativecommons.org/licenses/by-nc-nd/4.0/).

diffusion and pseudodiffusion effects into account, which is an important factor to consider in the skeletal muscles, where diffusion is highly restricted orthogonally to the muscle fiber orientation [24]. These limitations may explain the difference in homogeneity of the maps.

The elevated F_p in the cervical spinal canal has also been reported in the lumbar and thoracic spinal canal [25] and could be explained by the physiological, slow CSF pulsation. Though it should be noted that the IVIM model assumes microscopic flow in a capillary network and hence is probably not ideal to describe the CSF pulsation. Moreover, on careful examination of the parametric map in Figs. Fig. 44 d and Fig. 55 b, there is a slight incongruence of the red, high-F_p area and the bright CSF signal, with some of the high-F_p area located more in the epidural fat. We presume that an additional factor contributing to the high F_p may be the blood flow in the epidural venous plexus, which is most largely developed in the anterior portion. Whether this effect could be used for other diagnostic purposes, i.e. for differentiation of intraspinal masses, is beyond the scope of this study.

The adenoma showed a low restriction of passive water diffusion (high D) when compared to the normal thyroid parenchyma of volunteers or of the contralateral side in the patient, which may be explained with larger cell size or smaller extracellular fluid space, i.e. poor vascularization [25, 26]. Benign focal lesions have been reported to show low ADC in conventional DWI, and malignant lesions typically show even lower ADC values as a result of the high cellularity [26]. Compared to these previous studies using conventional DWI, the proposed IVIM analysis additionally provides information on tissue perfusion potentially resulting in a better discrimination between benign and malignant lesions. A further application may be the use of IVIM for therapy response monitoring of nodular or diffuse thyroid pathologies. We believe that IVIM of the thyroid has some potential to increase accuracy and; thereby, minimize harm in the diagnostic workup of thyroid pathologies, but further prospective studies are needed to uncover the full value of thyroid IVIM-imaging.

Our study has several limitations. (i) The duration of our protocol with the acquisition of 12 b-values was fairly long (approx. 25 min) and in the current state would be difficult to implement as an additional sequence to an existing clinical neck MR protocol. However, the number of b-values may potentially be decreased without losing diagnostic accuracy, and such approaches have successfully been tested for IVIM. Moreover, the introduction of multi-band DWI sequences with simultaneous excitation of multiple slices with subsequent unaliasing of the acquired data have been shown to result in a dramatic decrease of acquisition time. In the future, such an approach may potentially be successfully applied for IVIM measurements. (ii) Another limitation of thyroid MRI with a large FOV is the

http://dx.doi.org/10.1016/j.heliyon.2017.e00239
2405-8440/© 2017 The Authors. Published by Elsevier Ltd. This is an open access article under the CC BY-NC-ND license (http://creativecommons.org/licenses/by-nc-nd/4.0/).

limited spatial resolution. In our study we used a relatively large FOV in order to be able to compare the thyroid characteristics with other anatomical structures. A reduced FOV potentially provides a better spatial resolution as reported by Lu et al. [13], though the increased spatial resolution poses further problems for IVIM acquisitions. Firstly, in order to obtain a sufficient signal-to-noise ratio (SNR), more acquisitions have to be performed as the SNR is directly proportional to the voxel volume, and subsequently an even longer measurement time as compared to our protocol would be necessary. Moreover, the examination with reduced FOV would be prone to folding artifacts in the phase encoding direction, which, however, could be compensated by zoomed echo-planar imaging with parallel transmission if the required MR scanner hardware is available.

(iii) ssEPI as used in the present study for IVIM is very sensitive to magnetic field inhomogeneities, which occur at soft tissue-air and soft tissue-bone interfaces in head and neck imaging. The parameters may thus be inaccurate for regions of the thyroid lobes bordering the trachea; and an evaluation of the isthmus, which happens to be very thin and unfavorably located between extracorporeal and tracheal air, is not possible.

(iv) Lastly, the IVIM approach is sensitive to movement in between the acquisition of the different b-values. For small movements compensation should be possible by the built-in proprietary software. From the consistency of our data between the subjects we infer that motion was not a serious issue in our cohort of healthy volunteers. Clinically, this could potentially constitute a problem when patients feel the need of excessive swallowing during the examination, since the thyroid may exhibit large movements together with the whole larynx (an effect usually exploited for manual palpation).

In conclusion, we demonstrated that IVIM measurements in the thyroid gland are feasible using the proposed protocol. The tissue characterization using IVIM provides biomarkers on cellular diffusion restriction and perfusion; thereby providing a more comprehensive description of tissue properties compared to conventional DWI.

Declarations

Author contribution statement

Anton S. Becker: Conceived and designed the experiments; Performed the experiments; Analyzed and interpreted the data; Contributed reagents, materials, analysis tools or data; Wrote the paper.

Tim Finkenstaedt: Analyzed and interpreted the data; Contributed reagents, materials, analysis tools or data; Wrote the paper.

http://dx.doi.org/10.1016/j.heliyon.2017.e00239
2405-8440/© 2017 The Authors. Published by Elsevier Ltd. This is an open access article under the CC BY-NC-ND license (http://creativecommons.org/licenses/by-nc-nd/4.0/).

Moritz C. Wurnig, Andreas Boss: Conceived and designed the experiments; Performed the experiments; Analyzed and interpreted the data; Contributed reagents, materials, analysis tools or data.

Funding statement

This research did not receive any specific grant from funding agencies in the public, commercial, or not-for-profit sectors.

Competing interest statement

The authors declare no conflict of interest.

Additional information

No additional information is available for this paper.

References

[1] G.H. Tan, H. Gharib, Thyroid Incidentalomas: Management Approaches to Nonpalpable Nodules Discovered Incidentally on Thyroid Imaging, Ann. Intern. Med. 126 (3) (1997) 226–231.

[2] E. Tomimori, F. Pedrinola, H. Cavaliere, M. Knobel, G. Medeiros-Neto, Prevalence of incidental thyroid disease in a relatively low iodine intake area, Thyroid 5 (4) (1995) 273–276.

[3] D.S. Cooper, G.M. Doherty, B.R. Haugen, et al., Revised American Thyroid Association management guidelines for patients with thyroid nodules and differentiated thyroid cancer, Thyroid 19 (11) (2009) 1167–1214.

[4] E.L. Mazzaferri, S.M. Jhiang, Long-term impact of initial surgical and medical therapy on papillary and follicular thyroid cancer, Am. J. Med. 97 (5) (1994) 418–428.

[5] B. McIver, I.D. Hay, D.F. Giuffrida, et al., Anaplastic thyroid carcinoma: A 50-year experience at a single institution, Surgery 130 (6) (2001) 1028–1034.

[6] E.L. Mazzaferri, Management of a solitary thyroid nodule, N. Engl. J. Med. 328 (8) (1993) 553–559.

[7] D.Y. Yoon, S.K. Chang, C.S. Choi, et al., The Prevalence and Significance of Incidental Thyroid Nodules Identified on Computed Tomography, J. Comput. Assist. Tomogr. 32 (5) (2008) 810–815.

[8] E. Ben-David, N. Sadeghi, M.K. Rezaei, et al., Semiquantitative and Quantitative Analyses of Dynamic Contrast-Enhanced Magnetic Resonance

 http://dx.doi.org/10.1016/j.heliyon.2017.e00239

2405-8440/© 2017 The Authors. Published by Elsevier Ltd. This is an open access article under the CC BY-NC-ND license (http://creativecommons.org/licenses/by-nc-nd/4.0/).

Imaging of Thyroid Nodules, J. Comput. Assist. Tomogr. 39 (6) (2015) 855–859.

[9] S. Unnikrishnan, A.L. Klibanov, Microbubbles as Ultrasound Contrast Agents for Molecular Imaging: Preparation and Application, Am. J. Roentgenol. 199 (2) (2012) 292–299.

[10] M. Ghofrani, D. Beckman, D.L. Rimm, The value of onsite adequacy assessment of thyroid fine-needle aspirations is a function of operator experience, Cancer 108 (2) (2006) 110–113.

[11] J. Valentin, The 2007 recommendations of the international commission on radiological protection, Elsevier Oxford, 2007.

[12] C. Lundh, M.M. Nordén, M. Nilsson, E. Forssell-Aronsson, Reduced Iodide Transport (Stunning) and DNA Synthesis in Thyrocytes Exposed to Low Absorbed Doses from 131I *in vitro*, J. Nucl. Med. 48 (3) (2007) 481–486.

[13] Y. Lu, V. Hatzoglou, S. Banerjee, et al., Repeatability Investigation of Reduced Field-of-View Diffusion-Weighted Magnetic Resonance Imaging on Thyroid Glands, J. Comput. Assist. Tomogr. 39 (3) (2015) 334–339.

[14] H.F. Shi, Q. Feng, J.W. Qiang, R.K. Li, L. Wang, J.P. Yu, Utility of diffusion-weighted imaging in differentiating malignant from benign thyroid nodules with magnetic resonance imaging and pathologic correlation, J. Comput. Assist. Tomogr. 37 (4) (2013) 505–510.

[15] C. Schraml, A. Boss, P. Martirosian, N.F. Schwenzer, C.D. Claussen, F. Schick, FAIR true-FISP perfusion imaging of the thyroid gland, J. Magn. Reson Imaging 26 (1) (2007) 66–71.

[16] C. Schraml, K. Mussig, P. Martirosian, et al., Autoimmune thyroid disease: arterial spin-labeling perfusion MR imaging, Radiology 253 (2) (2009) 435–442.

[17] C. Eberhardt, M.C. Wurnig, A. Wirsching, C. Rossi, et al., Intravoxel incoherent motion analysis of abdominal organs: computation of reference parameters in a large cohort of C57Bl/6 mice and correlation to microvessel density, Magn. Reson. Mater. Phy. 29 (2016) 751.

[18] D. Le Bihan, E. Breton, D. Lallemand, M.L. Aubin, J. Vignaud, M. Laval-Jeantet, Separation of diffusion and perfusion in intravoxel incoherent motion MR imaging, Radiology 168 (2) (1988) 497–505.

[19] D. Le Bihan, Intravoxel incoherent motion imaging using steady-state free precession, Magn. Reson. Med. 7 (3) (1988) 346–351.

 http://dx.doi.org/10.1016/j.heliyon.2017.e00239

2405-8440/© 2017 The Authors. Published by Elsevier Ltd. This is an open access article under the CC BY-NC-ND license (http://creativecommons.org/licenses/by-nc-nd/4.0/).

[20] D. Le Bihan, R. Turner, The capillary network: a link between IVIM and classical perfusion, Magn. Reson. Med. 27 (1) (1992) 171–178.

[21] C. Federau, P. Maeder, K. O'Brien, P. Browaeys, R. Meuli, P. Hagmann, Quantitative measurement of brain perfusion with intravoxel incoherent motion MR imaging, Radiology 265 (3) (2012) 874–881.

[22] M.C. Wurnig, O.F. Donati, E. Ulbrich, L. Filli, D. Kenkel, H.C. Thoeny, A. Boss, Systematic analysis of the intravoxel incoherent motion threshold separating perfusion and diffusion effects: Proposal of a standardized algorithm, Magn. Res. Med. 74 (5) (2015) 1414–1422.

[23] L. Filli, A. Boss, M.C. Wurnig, D. Kenkel, G. Andreisek, R. Guggenberger, Dynamic intravoxel incoherent motion imaging of skeletal muscle at rest and after exercise, NMR Biomed. 28 (2) (2015) 240–246.

[24] D.C. Karampinos, K.F. King, B.P. Sutton, J.G. Georgiadis, Intravoxel partially coherent motion technique: characterization of the anisotropy of skeletal muscle microvasculature, J. Magn. Reson. Imaging 31 (4) (2010) 942–953.

[25] L. Filli, M.C. Wurnig, R. Luechinger, C. Eberhardt, R. Guggenberger, A. Boss, Whole-body intravoxel incoherent motion imaging, Eur. Radiol. 25 (7) (2015) 2049–2058.

[26] G. Erdem, T. Erdem, H. Muammer, et al., Diffusion-weighted images differentiate benign from malignant thyroid nodules, J. Magn. Reson. Imaging 31 (1) (2010) 94–100.

 http://dx.doi.org/10.1016/j.heliyon.2017.e00239

2405-8440/© 2017 The Authors. Published by Elsevier Ltd. This is an open access article under the CC BY-NC-ND license (http://creativecommons.org/licenses/by-nc-nd/4.0/).